Mechanics of Linear Microcracking in Trabecular Bone

Max A. Hammond[1], Joseph M. Wallace[2], Matthew R. Allen[2,3], Thomas Siegmund[1*]

[1] Department of Mechanical Engineering, Purdue University, West Lafayette, IN, USA
[2] Department of Biomedical Engineering, Indiana University-Purdue University at Indianapolis, IN, USA
[3] Department of Anatomy and Cell Biology, Indiana University School of Medicine, IN, USA

Abstract

Microcracking in trabecular bone is responsible both for the mechanical degradation and remodeling of the trabecular bone tissue. Recent results on trabecular bone mechanics have demonstrated that bone tissue microarchitecture, tissue elastic heterogeneity and tissue-level mechanical anisotropy all should be considered to obtain detailed information on the mechanical stress state. The present study investigated the influence of tissue microarchitecture, tissue heterogeneity in elasticity and material separation properties, and tissue-level anisotropy on the microcrack formation process. Microscale bone models were executed with the extended finite element method. It was demonstrated that anisotropy and heterogeneity of the bone tissue contribute significantly to bone tissue toughness and the resistance of trabecular bone to microcrack formation. The compressive strain to microcrack initiation was computed to increase by a factor of four from an assumed homogeneous isotropic tissue to an assumed anisotropic heterogenous tissue.

Keywords:

Trabecular bone, Anisotropy, Heterogeneity, Stress analysis, Microcracking, XFEM

*** Corresponding Author:**
T. Siegmund,
School of Mechanical Engineering Purdue University
585 Purdue Mall West Lafayette, IN 47907, USA
Tel.: +1-765-494-9766
Fax: +1-765-496-7536
Email: siegmund@purdue.edu

1. Introduction

Microcracks form in vivo and are considered central to the understanding of bone mechanical degradation (Frost, 1960; Wenzel et al., 1996; Verborgt et al., 2000; Acevedo et al., 2018). Images of 2D and 3D (Lambers et al., 2013) histological sections, scanning electron microscopy (Thurner et al., 2007), contrast enhanced micro-computed tomography (μCT) imaging (Wang et al., 2007) and synchrotron imaging (Larrue et al., 2011) all reveal the prominence of the linear microcrack configuration. Figure 1A-B each depict a single trabeculae containing a linear microcrack. In Fig. 1A the microcrack is shown in a basic Fuchsin stained histological section under fluorescent light, while in Fig. 1B the similar microcrack is visualized by a μCT scan of bone stained with $BaSO_4$. Both images demonstrate that the crack surfaces of linear microcracks in trabecular bone are predominantly aligned with the local trabecular bone surface. Figure 1C depicts a μCT scan image of multiple trabeculae with linear microcracks broadly distributed throughout the tissue.

Relationships between microcrack parameters and mechanical loading, and/or bone biological conditions have been established in several studies (Mori et al., 1997; Allen and Burr, 2007; Lambers et al., 2013). Yet, at the same time, the biomechanical processes leading to microcrack formation are not fully understood. One finding relates microcrack formation to mechanical strains (Goff et al., 2015), but another study finds no clear evidence for such a relationship (Tassani et el., 2018). Recent data have described the influence of tissue heterogeneity on microcracking (Torres et al., 2016), however, the effects of combined heterogeneity and anisotropy are not known.

Computational simulations leading to discrete microcrack formation can be conducted within the framework of cohesive material separation, either through the use of a cohesive element formulation (Planas et al., 2002) or in the context of the extended finite element method (XFEM) (Sukumar et al., 2015). The cohesive material separation approach was used in investigations of crack initiation and propagation in bone across length scales. In (Siegmund et al., 2008) the approach was applied to the nanoscale mineralized collagen fibril, (Hamed and Jasiuk, 2013) applied the approach up to microscale lamellar bone, while (Abdel-Wahab et al., 2012; Besdo and Vashishth, 2012; Feerick et al., 2013) considered this approach in mesoscale cortical bone. Tomar (2008) applied the cohesive modeling technique in an investigation of microcrack formation in trabecular bone under dynamic loading and considering a 2D model. Here a XFEM approach is applied in 3D to allow for largely mesh-independent cracking.

We hypothesized that the processes of microcrack formation and tissue resistance against microcracking are intrinsically related to the tissue biomechanical heterogeneity and tissue anisotropy of the deformation/tissue separation response. In (Hammond et al., 2018) we have demonstrated that both tissue heterogeneity and tissue anisotropy have significant influence on the mechanical stress state in trabecular bone. Therefore, we tested our hypothesis by comparing the outcomes of finite element simulations of microcrack formation under four different combinations of tissue biomechanical properties varying tissue heterogeneity and anisotropy.

2. Materials and Methods

2.1. Sample and Model Preparation

A trabecular core was obtained from the distal femur of a human cadaver through the Indiana University School of Medicine Anatomical Education Donor Program. The trabecular core was imaged with a Skyscan 1172 μCT system (Bruker μCT, Kontich, Belgium) with an isotropic voxel size of 5.88 μm. NRecon (Bruker μCT) was used to reconstruct voxels with attenuation coefficients in the 0 to 0.11 mm^{-1} range, and Dataviewer (Bruker μCT) was used to vertically align the images. The sample had a bone volume fraction of 18.2% and an average trabecular thickness of 68.3 μm. Manufacturer supplied hydroxyapatite phantoms of 250 and 750 kg/m^3 were used to calibrate the mineral density (ρ) for each image grayscale (GS) value. The linear relationship $\rho_{GS} = 11.1\ kg/m^3 \times GS - 255\ kg/m^3$, derived from a linear fit of the grayscales of the phantoms, was used to assign spatially varying tissue density values to each element. Collagen lamellae are known to be aligned with the local surface (Reznikov et al., 2015; Georgiadis et al., 2016). The anisotropy of the tissue is defined by computing the local normal (i) to the tissue surface (j, k) as defined in (Hammond et al., 2018).

Using CTAn (Bruker μCT), regions of interest were selected to isolate a domain (280 μm x 275 μm x 223 μm) containing a single rod-like trabecula (L_{trab}=160 μm trabecular length, 90 μm minimum trabecular thickness), and a cube bone core (side length H_{core}=3000 μm) from the center of the trabecular compartment. Gaussian smoothing was applied to the regions of interest. The Otsu method was used to determine the optimal threshold to separate bone from marrow. ScanIP (Simpleware, Montainview, CA) was used to create a free continuum finite element mesh and to associate the average grayscale of the bone tissue in each region of interest.

For the single trabeculae model, loading under displacement control was achieved by fully constraining one model face while applying a transverse displacement to the opposite face. The finite element mesh consisted of 72,614 fully integrated 10 node tetrahedral elements. At the smallest cross section, the mesh consisted of 25 elements across the section.

For the bone core models, a transaxial compressive displacement was applied to the nodes on the upper transaxial surface. All nodes on the lower transaxial surface were fully constrained. All other external surfaces remained free. The finite element mesh consisted of 2,544,945 fully integrated 10 node tetrahedral elements. For the smallest trabeculae, the mesh consisted of at least 4 or 5 elements across the section.

2.2. Tissue Biomechanical Properties

Trabecular bone tissue was considered as a linear elastic solid with microcracks nucleating and growing. Simulations of elastic deformation, microcrack initiation and microcrack growth were carried out by the use of a non-linear, large displacement finite element method with enriched elements applying principles of the extended finite element method (XFEM) with multisite microcracking. Four models were created for both the single trabeculae and the bone core (Fig. 2). Tissue elastic and failure properties are allocated in the models with spatial heterogeneity and anisotropy. In anisotropic models, transversely isotropic elastic properties were defined as $2E_i$ =

$E_j = E_k$, $v_{jk} = 1.25v_{ji} = 0.37$, and $G_{jk} = 1.5G_{ji}$. Ratios between the moduli i-axis and the jk-plane are similar to those observed experimentally (Reisinger et al., 2011). Isotropic models had values of E, v, and G equal to those in the plane of symmetry (E_j, v_{jk}, and G_{jk}). In heterogeneous models, E_i and E were adjusted based on a scaling factor derived from the ratio of the modulus calculated using the average local density within each element and the modulus calculated using the global average density in the model. Following models (Rho et al., 1995), the relationship $E/E_0 = (0.912\ \mathrm{m^2/s^2} \times \rho_{GS} - 66.2)$ was used to convert each local density value to the respective normalized local isotropic modulus. Heterogeneity did not alter v_{jk} or v, but varying E_i or E dictated the effect of heterogeneity on G_{jk} or G, respectively. The scan data lead to density values ranging between $\min(\rho_{GS})$=777.3 kg/m^3 and $\max(\rho_{GS})$=1576.5 kg/m^3 with an average value density $\mathrm{avg}(\rho_{GS})$=1168 kg/m^3.

Two microcrack formation criteria are considered. In isotropic tissue models, microcracks initiate if the ratio of maximum tensile principal stress ($\sigma_{p,\max}$) to microcrack ignition strength $\sigma_{\max}$ fulfilled the criterion f=1:

$$f = \left\{ \frac{\left\langle \sigma_{p,\max} \right\rangle}{\sigma_{\max}} \right\}, \quad \left\langle \sigma_{p,\max} \right\rangle = \begin{cases} \sigma_{p,\max}, \sigma_{p,\max} > 0 \\ 0, \sigma_{p,\max} < 0 \end{cases} \tag{1}$$

Microcracks are then formed in a plane normal to the maximum principal stress direction computed from the local stress state. In anisotropic tissue models, microcracks initiate if the maximum nominal stress criterion is fulfilled, f=1:

$$f = \max\left\{ \frac{\left\langle t_i \right\rangle}{\sigma_{\max}}, \frac{t_j}{\sigma_{\max}}, \frac{t_k}{\sigma_{\max}} \right\}, \quad \left\langle t_i \right\rangle = \begin{cases} t_i, t_i > 0 \\ 0, t_i < 0 \end{cases} \tag{2}$$

Here, t_i is the normal traction in the direction of the trabecular surface outward normal (i), and t_j and t_k are the respective shear tractions. The microcrack initiation strength was related to the local elastic modulus and is characterized by a reference strain ε_0. In isotropic models $\varepsilon_0 = \sigma_{\max}/E$=(1/500), and in anisotropic models $\varepsilon_0 = \sigma_{\max}/E_i$ =(1/500). Once a microcrack initiation criterion is fulfilled, the tractions across the microcrack decline linearly until a critical separation δ_c is reached where traction vanish. This corresponds to the situation of microcracks bridged by mineralized collagen fibrils (Thurner et al., 2007). The microcrack toughness is $G_c = (1/2)\sigma_{\max} \cdot \delta_c$ =0.5 MPa mm, and that value is constant in all cases. In heterogeneous models, both the modulus and strength increase from near surface domains the interior domains by a factor of two. At the same time the value of δ_c declines from the trabecular surface into the trabecular interior by a factor of two. Thus, near surface domains are less brittle (low strength and slow decline in traction with microcrack opening) while the trabecular interior is more brittle (high strength and rapid decline the traction with microcrack opening). Friction between microcrack surfaces is neglected. Following (Lu et al., 1994) this should have minor influence on the energy release rates at the microcrack tips.

2.3. Analysis

Figure 3 depicts the single trabeculae and the bone core model, including the displacement boundary conditions and details of the FE mesh. The single trabeculae was loaded under an applied eccentric displacement U_{appl} such that the applied strain is $\varepsilon_{appl}=U_{appl}/L_{trab}$. The bone core model was loaded under an applied compressive displacement U_{appl} along the main trabecular direction such that the applied strain is $\varepsilon_{appl}=U_{appl}/H_{core}$. For elements where the microcrack initiation criterion was fulfilled ($f = 1$) the signed distance function from each node to the microcrack plane, the displacement of each node, and the energy dissipation due to the microcrack was recorded. Stress and strain values were extrapolated to the crack tip to determine if both the damage initiation criterion is satisfied and to determine the crack propagation direction. The location of the microcrack plane within each element was calculated from the initial coordinates of each node, the nodal displacements, and the signed distance function to the microcrack plane. Subsequently, the microcrack area for each individual element is obtained using the $f = 1$ criterion. Each element was separated into its respective microcrack region allowing the total number of microcracks and individual microcrack areas to be determined. The total microcrack area and total energy dissipation due to microcracking were obtained. Regions within 20 μm of the applied boundary conditions in the single trabecula and 200 μm of the applied boundary conditions in the core were excluded from the data analysis to remove the effects of stress concentrations from the application of the boundary conditions.

The commercial FE code ABAQUS/Standard v2017 (Dassault Systèmes SIMULIA, Johnston, RI), was employed for the simulation and the visualization. Model creation and post processing was conducted in MATLAB R2018a (Mathworks, Nantick, MA). Simulations were stopped when the displacement necessary to compute a further increment was less than 10 pm in the single trabecula models and 30 fm in the bone core models.

3. Results

3.1. Microcracking in the Single Trabecula Model

In the single trabecula models, both IsoHmg and IsoHtg models resulted in the formation of transverse cracks at the site of minimal trabecular thickness (Fig. 4 A-B), with the microcrack initiating at the trabecular surface and propagating towards the interior in both cases. In AnisoHmg and AnsioHtg models, the morphology of the microcrack was contained within the interior of the trabecula with the crack surface parallel to the trabecula surface (Fig. 4 C-D). Heterogeneity altered the site of microcrack initiation and subsequent growth in the anisotropic models. When the tissue was assumed as homogeneous, the microcrack was located deep into the trabecula interior (18 μm away from the surface), while for the heterogeneous tissue model the microcrack was close to the trabecula surface (3.3 μm away from the surface).

Figure 5A depicts the computed evolution of the microcrack relative to normalized applied strain $\varepsilon_{appl}/\varepsilon_0$. The transverse microcracks in the IsoHmg and IsoHtg scenerios initiated at small values of $\varepsilon_{appl}/\varepsilon_0$ and subsequently grew rapidly in both cases. Anisotropy was found to delay microcrack initiation. The value of $\varepsilon_{appl}/\varepsilon_0$ at microcrack initiation for the AnisoHmg model was

7.5 times that for the IsoHmg model, and for the AnisoHtg model 3 times that of the IsoHtg (Fig. 5A). While heterogeneity did not affect microcrack initiation in the isotropic models, its effect in anisotropic models was notable. For the AnisoHtg model, microcrack growth occurred much earlier than in the AnisoHmg model, but the subsequent crack growth was negligible up to the crack initiation of the AnsioHtg model. In the isotropic models the predicted microcrack growth rate was high instantaneously, a feature of brittle failure. In the anisotropic models, the predicted growth rate following initiation was low and only later increased, a feature of a damage tolerant system. Combined effects between anisotropy and heterogeneity on microcrack growth were strongest in the energy dissipated per microcrack area data. At a microcrack area of 0.0015 mm^2, there was over a 3-fold higher energy dissipation predicted for the AnisoHtg case compared to the AnisoHmg case. This finding indicates a substantive difference in the progression of material separation in the period beyond microcrack initiation. On the other hand, the effect of heterogeneity in the isotropic models was minimal (Fig. 5B).

3.2 Microcracking in the Bone Core Model

Examples of predicted microcracks in the bone core models are depicted in Fig. 6. For the IsoHmg model, Fig. 6 A, transverse microcracks are formed, consistent with the single trabecula model, Fig. 4 A-B. For the AnisoHmg model, Fig. 6B, microcracks following the trabecular surface are formed, consistent with the single trabecula model, Fig. 4 C-D.

Figure 7A depicts the cumulative microcrack area in dependence of $\varepsilon_{appl}/\varepsilon_0$ for the bone core models and all four tissue biomechanical models. Values for the applied strain at crack initiation ($\varepsilon_{ini}/\varepsilon_0$) are given. In the homogenous models, the first microcrack initiation occurred again early on and the subsequent microcrack area growth rate is high instantaneously after crack initiation. For the anisotropic models, the first microcrack initiation is delayed relative to the isotropic cases. Subsequently, further microcrack area accumulation is slow and only later increases to the growth rates of the isotropic cases. The increases in microcrack area were driven by microcrack growth in the isotropic models. However, for the anisotropic models, the microcrack area increases through both the formation of additional microcracks and the growth of individual microcracks (Fig. 7B). While the energy dissipation per total microcrack area was higher for the anisotropic models than for the isotropic models (Fig. 7 C). Combining data from Fig. 7 B and Fig. 7 C, the energy dissipation per microcrack can be estimated. In AnisoHmg model the energy dissipated per microcrack was approximately 1.5 times higher than in the AnisoHtg model while the difference in the isotropic models was not substantial.

Figure 8 depicts the spatial distribution of microcrack lengths (numbered from largest to smallest) at a total microcrack area of approximately $2.5x10^{-3}$ mm^2 in all models. Comparing predictions for the isotropic and anisotropic models, anisotropy drastically altered the location of microcracks and increased number of microcracks present. Heterogeneity altered the relative sizes of each microcrack within a model, but overall if a microcrack was present in a location in the homogeneous model a corresponding microcrack was also present in the heterogeneous model in both the isotropic and anisotropic case. Heterogeneity did not alter the location of the initial

microcrack in the isotropic model but did in the anisotropic model. In the anisotropic models, several locations had multiple discrete and small microcracks in close proximity and this effect was more pronounced in the heterogeneous anisotropic model.

Figure 9 summarizes the growth for individual microcracks with respect to the normalized post-initiation strain $(\varepsilon_{appl}- \varepsilon_{ini})/\varepsilon_0$. For the isotropic models with the maximum principal stress criterion, the growth of the initial transverse microcrack dominates over all other microcracks formed at a later stage. Although secondary microcracks formed, these remained comparatively small. This dominating effect was found to be most apparent in the isotropic homogeneous case. For the anisotropic models, the initial microcrack did not become dominant. Several microcracks formed at a later time are of similar length (AnisoHmg) or even longer (AnisoHtg) than the initial microcrack. In addition, several smaller microcracks formed.

4. Discussion

The present computation supported the hypothesis that microcracking is related to the biomechanical tissue anisotropy (i.e. the transverse isotropic moduli and the microcrack initiation criterion imposed on the tissue anisotropy) and heterogeneity (i.e. the spatially varying moduli and microcrack initiation strength). The hypothesis of the role of anisotropy was confirmed: only the models with anisotropy accounted for in the microcrack initiation criterion predicted the formation of linear microcracks (Fig. 4 C-D, Fig. 5 B) as well as a wide spatial distribution of similar-sized microcracks (Fig. 8 C-D). Heterogeneity in the tissue was observed to locate microcracks closer to the experimentally observed locations near and parallel to the trabecular surface.

The deformation of trabeculae in a bone core involves complex stress states. Microcrack initiation in trabecular bone can be discussed in the context of the mechanics of axial deformation, bending and shear deformation, as well as torsion of individual trabecula. The mechanics of such stress and deformation problems on basic geometries (circular rods) is well understood. However, the specifics of the biomechanical properties of the trabecular bone tissue and the microarchitecture impose substantive complexities. In the end, trabeculae are curved members with near circular cross section of varying diameter across the span, possessing radially graded mechanical properties as well as radial anisotropy. Structural members with low modulus at the surface and higher modulus in the interior can possess flexural stress distributions where the maximum normal stress no longer occurs at the surface (Aldousari, 2017). This effect has been described as a shielding effect in bone (Torres et al., 2016). Tissue heterogeneity is responsible for the alteration of initiation site for linear microcrack initiation. Then the question arises whether the initiation of linear microcracks is due to shear tractions or transversal normal tractions. Additional numerical experiments on the single trabeculae model with either shear or normal separation blocked, reveal that linear microcrack initiation is transverse shear dominated. In homogeneous and isotropic beams, the maximum shear stress arises at the neutral axis, and is intrinsically connected to the linear dependence of the flexural stress in dependence on the distance from the neutral axis. This is similar to the anisotropic-homogenous case considered. The tissue heterogeneity alters the flexural stress state (Aldousari, 2017) such that a local maximum in

flexural stresses occurs subsurface, and that local maximum is then linked to secondary maximum in transverse shear stress near the surface. As the shear strength is low due to the tissue heterogeneity, linear microcrack initiation is predicted in the trabecular interior close to the trabecular surface. The radial symmetry of anisotropy and heterogeneity are responsible for the microcrack growth into internal microcracks with surfaces parallel to the trabecular surfaces. For the isolated trabeculae, this effect was not effective in delaying microcrack initiation (Fig. 5A). Heterogeneity did, however, increase the energy dissipation during microcrack growth in both the transverse and the linear microcracks (Fig. 6 B) in the single trabeculae model. No conclusive evidence of similar effects on the bone core model could be established. Heterogeneity increased the number of microcracks (AnisoHm vs. AnisoHtg. Fig. 7 B), but the respective energy dissipation was higher for the AnisoHmg case. Microcrack evolution in the single trabeculae model and the core model show similar trends in terms of microcrack area evolution in that anisotropy delays crack initiation and reduces microcrack area accumulation rate, Figs 6 A and 7 A. In the single trabeculae model, however, all damage is due to a single defect, while in the core model multiple microcracks occur, Fig. 7 B. The energy dissipation in the core, Fig 7 C, is thus a cumulated measure over all microcracks while in the single trabeculae this measure only accounts for a single microcrack, Fig. 6 B. Transverse microcracks were found to initiate from the trabecular surface and thus are always associated with the location of maximum strain. For linear microcracks the spatial association with the location of maximum strains depends on the tissue heterogeneity. If a trabecula is homogeneous in elastic properties the microcrack location is not associated with the maximum strain. However, if the tissue elastic properties are heterogeneous, microcrack location and maximum strain location are closely associated. This explains the experimental findings of microcrack-strain association measured in (Goff et al., 2015).

The present model approach can be useful in studies of the effects of various osteoporosis treatments on bone microcrack evolution (Allen and Burr, 2007). This can be accomplished by treatment related parametric modifications of model input parameters. Furthermore, the model can also be used in studies of biomedical devices such as bone screws. Thereby, this present approach would augment prior demonstrated approaches (Wirth et al., 2012) with information in local damage evolution."

Recent nanopillar compression experiments (Luczynski et al., 2015; Schwiedrzik et al., 2017) have demonstrated modulus to strength ratios in the range of 50 to 100. Considering that these values where obtained on nanopillars which often exhibit size dependent strengthening and the use of a 0.4% off set criterion for the strength, it is argued that the modulus to strength ratio of 500 provides at least a lower bound value. The present implementation of the extended finite element method with multi-site cracking did not allow for microcrack coalescence or intersection. However, at the loads considered here, microcracks were still of dilute concentration and no interaction was near occurring. The tissue anisotropy was transversely isotropic but no principle barrier exists to a fully orthotropic extension of the model. There is no principal limitation to the extension of the model to incorporate such data if available in the future. Microcrack formation was exclusively predicted by either the maximum principal stress or the maximum nominal stress

criterion. A model where the two criteria compete could further elucidate the microcrack formation process and demonstrate the competition between linear and transverse microcracks. However, as linear microcracking is a major morphology noted in various studies, the present model and the maximum nominal stress criterion in conjunction with the transversely isotropic orientation distribution appears as a viable choice for investigations of microcrack formation.

5. Conclusion

The present study demonstrated that trabecular tissue anisotropy—reflected in the spatial distribution of the tissue elastic response, the anisotropy of the elastic properties and the directional maximum nominal stress microcrack initiation criterion—plays an important role in the formation of linear microcracks in trabecular bone. Only if all such features are accounted for in a model of microcrack formation, is it possible to predict the shape and distributed microcracking typically observed in trabecular bone.

Acknowledgements

This material was based upon work supported by the National Science Foundation under Grant No. 1643164. This work used the Extreme Science and Engineering Discovery Environment (XSEDE), which is supported by National Science Foundation grant number ACI-1548562. Carmen Herrera contribution to the 3D images of microcracks is acknowledged.

Conflict of Interest Statement

The authors declare that no conflict of interests exist.

References

Abdel-Wahab, A.A., Maligno, A.R. and Silberschmidt, V.V. **Micro-scale modelling of bovine cortical bone fracture: analysis of crack propagation and microstructure using X-FEM.** *Comp Mat Sci* 2012; 52: 128-135.

Acevedo, C., Stadelmann, V.A., Pioletti, D.P., Alliston, T. and Ritchie, R.O. **Fatigue as the missing link between bone fragility and fracture.** *Nature Biomed Engng* 2018; 1.

Aldousari, S.M. **Bending analysis of different material distributions of functionally graded beam.** *Appl Phys A*, 2017;123:296.

Allen, M.R. and Burr, D.B. **Three years of alendronate treatment results in similar levels of vertebral microdamage as after one year of treatment.** *J Bone Mineral Res* 2007; 22:1759-1765.

Besdo, S. and Vashishth, D. **Extended Finite Element models of introcortical porosity and heterogeneity in cortical bone.** *Comp Mat Sci* 2012;64:301-305.

Elices, M.G.G.V., Guinea, G.V., Gomez, J. and Planas, J. **The cohesive zone model: advantages, limitations and challenges.** *Engng Fract Mech* 2002;69:137-163.

Feerick, E.M., Liu, X.C. and McGarry, P. **Anisotropic mode-dependent damage of cortical bone using the extended finite element method (XFEM).** *J Mech Behav Biomed Mater* 2013;20:77-89.

Frost, H.M. **Presence of microscopic cracks in vivo in bone.** *Henry Ford Hosp Med Bull* 1960;8:25-35.

Georgiadis, M., Guizar-Sicairos, M., Gschwend, O., Hangartner, P., Bunk, O., Müller, R., Schneider, P. **Ultrastructure organization of human trabeculae assessed by 3D sSAXS and relation to bone microarchitecture.** *PLOS ONE* 2016;11:e0159,838.

Goff, M.G., Lambers, F.M., Nguyen, T.M., Sung, J., Rimnac, C.M. and Hernandez, C.J. **Fatigue-induced microdamage in cancellous bone occurs distant from resorption cavities and trabecular surfaces.** *Bone* 2015;79:8-14.

Goff, M.G., Lambers, F.M., Sorna, R.M., Keaveny, T.M. and Hernandez, C.J. **Finite element models predict the location of microdamage in cancellous bone following uniaxial loading.** *J Biomech* 2015;48:4142-4148.

Hamed, E. and Jasiuk, I. **Multiscale damage and strength of lamellar bone modeled by cohesive finite elements.** *J Mech Behav Biomed Mat* 2013;28:94-110.

Hammond, M.A., Wallace, J.M., Allen, M.R. and Siegmund, T. **Incorporating tissue anisotropy and heterogeneity in finite element models of trabecular bone altered predicted local stress distributions.** *Biomech Model Mechanobio* 2018;17:605-614.

Lambers, F.M., Bouman, A.R., Rimnac, C.M. and Hernandez, C.J. **Microdamage caused by fatigue loading in human cancellous bone: relationship to reductions in bone biomechanical performance.** *PLoS One* 2013;8:e83662.

Larrue, A., Rattner, A., Peter, Z.A., Olivier, C., Laroche, N., Vico, L. and Peyrin, F. **Synchrotron radiation micro-CT at the micrometer scale for the analysis of the three-dimensional morphology of microcracks in human trabecular bone.** *PLoS One* 2011;6:e21297.

Lu, T.J., Xia, Z.C. and Hutchinson, J.W. **Delamination of beams under transverse shear and bending.** *Mater Sci Eng A* 1994;188:103-112.

Luczynski, K.W., Steiger-Thirsfeld, A., Bernardi, J., Eberhardsteiner, J. and Hellmich, C., 2015. **Extracellular bone matrix exhibits hardening elastoplasticity and more than double cortical strength: Evidence from homogeneous compression of non-tapered single micron-sized pillars welded to a rigid substrate**. *J Mech Behav Biomed Mater*, 2015;52,51-62.

Mori, S., Harruff, R., Ambrosius, W. and Burr, D.B. **Trabecular bone volume and microdamage accumulation in the femoral heads of women with and without femoral neck fractures**. *Bone* 1997;21:521-526.

Reisinger, A.G., Pahr, D.H., Zysset, P.K. **Principal stiffness orientation and degree of anisotropy of human osteons based on nanoindentation in three distinct planes**. *J Mech Behav Biomed Mat* 2011;4:2113–2127.

Reznikov, N., Chase, H., Brumfeld, V., Shahar, R., Weiner, S. **The 3D structure of the collagen fibril network in human trabecular bone: Relation to trabecular organization**. *Bone* 2015;71:189–195.

Rho, J.Y., Hobatho, M.C., Ashman, R.B. **Relations of mechanical properties to density and CT numbers in human bone**. *Med Eng Phys* 1995;17:347–355.

Schwiedrzik, J., Taylor, A., Casari, D., Wolfram, U., Zysset, P. and Michler, J., 2017. **Nanoscale deformation mechanisms and yield properties of hydrated bone extracellular matrix.** *Acta Biomat 2017;60:*302-314.

Siegmund, T., Allen, M.R. and Burr, D.B. **Failure of mineralized collagen fibrils: modeling the role of collagen cross-linking**. *J Biomech* 2008;41:1427-1435.

Sukumar, N., Dolbow, J.E. and Moës, N. **Extended finite element method in computational fracture mechanics: a retrospective examination**. *Int J Fract* 2015;196:189-206.

Tassani, S., Pani, M., Noailly, J. and Gonzalez Ballester, M.A. **Trabecular fracture zone might not be the higher strain region of the trabecular framework**. Front Mat 2018;5: 6.

Thurner, P.J., Erickson, B., Jungmann, R., Schriock, Z., Weaver, J.C., Fantner, G.E., Schitter, G., Morse, D.E. and Hansma, P.K. **High-speed photography of compressed human trabecular bone correlates whitening to microscopic damage**. *Eng Fract Mech* 2007;74:1928-1941.

Tomar, V. **Modeling of dynamic fracture and damage in two-dimensional trabecular bone microstructures using the cohesive finite element method**. *J Biomech Eng* 2008;130:021021.

Torres, A.M., Matheny, J.B., Keaveny, T.M., Taylor, D., Rimnac, C.M. and Hernandez, C.J. **Material heterogeneity in cancellous bone promotes deformation recovery after mechanical failure**. *Proc Nat Acad Sci* 2016;113:2892-2897.

Verborgt, O., Gibson, G. J., and Schaffler, M. B. **Loss of osteocyte integrity in association with microdamage and bone remodeling after fatigue in vivo**. *J Bone Mineral Res* 2000;15:60-67.

Wang, X., Masse, D.B., Leng, H., Hess, K.P., Ross, R.D., Roeder, R.K. and Niebur, G.L. **Detection of trabecular bone microdamage by micro-computed tomography.** *J Biomech* 2007;40:3397-3403.

Wenzel, T.E., Schaffler, M.B. and Fyhrie, D.P. **In vivo trabecular microcracks in human vertebral bone.** *Bone* 1996;19:89-95.

Wirth, A.J., Müller, R. and van Lenthe, G.H. **The discrete nature of trabecular bone microarchitecture affects implant stability.** *J Biomech* 2012;45:1060-1067.

Figure Captions

Figure 1. Linear microcracks in trabecular bone often follow the geometry of the trabecular surface A) Micrograph of a linear microcrack (arrow) stained using basic Fuchsin; B) μCT visualization of a microcrack (arrow) within a trabecula stained using $BaSO_4$; C) μCT visualization of the microcrack (arrows) spatial distribution in a trabecular bone core stained using $BaSO_4$.

Figure 2: Model cases considered: (a) Model case IsoHmg: the bone tissue is considered as elastic isotropic, failing following the maximum principal stress criterion and as homogeneous; (b) Model case IsoHtg: the bone tissue is considered as elastic isotropic, failing following the maximum principal stress criterion and as heterogeneous; (c) Model case AnisoHmg: the bone tissue is considered as elastic transversely isotropic, failing following the maximum nominal stress criterion with direction imposed by the fibril orientation and as homogeneous; (d) Model case AnisoHtg: the bone tissue is considered as elastic transversely isotropic, failing following the maximum nominal stress criterion with direction imposed by the fibril orientation and as heterogeneous. In the schematic drawings gray scales indicate domains of constant tissue density and lines indicate fibril orientation.

Figure 3: Analysis models and schematic of boundary conditions: (a) single trabecula model, (b) core model with insert showing the finite element mesh.

Figure 4. Predicted microcrack morphology, single trabecula models with microcrack area 0.0015 mm^2: A) IsoHmg model and B) IsoHtg model: microcrack initiating (arrow) at the surface and propagating through the trabecular thickness; C) AnisoHmg model: microcrack initiating (arrow) within the trabecula, and with microcrack surface mostly parallel to the trabecular surface; D) AnisoHtg model: microcrack initiating (arrow) in the interior, and a microcrack surface following the trabecular surface. Insets in C) and D) depict cross-sections of the trabecula demonstrating a linear microcrack morphology and location.

Figure 5. Single trabecula model: A) Microcrack area vs. normalized applied strain: Anisotropy increased the strain at microcrack initiation and delayed microcrack growth in homogeneous and heterogeneous models compared to the isotropic cases while heterogeneity only had a noticeable effect in the anisotropic model; B) Energy dissipation vs. microcrack area: The interaction between anisotropy and heterogeneity produced a large increase in the energy dissipation per microcrack area in the AnisoHtg model.

Figure 6. Predicted microcrack morphology in the bone core models: A) IsoHmg model: transverse microcracks originating from the surface (black line) and propagating into the depth of the trabecula; B) AnisoHmg model: linear microcracks were predicted.

Figure 7. Total microcrack characteristics in the bone core models: A) Microcrack area vs. normalized applied strain: Anisotropy increased microcrack initiation strain and delayed microcrack growth, but heterogeneity reduced microcrack initiation strain; B) Microcrack area vs. number of cracks: Increases in microcrack area were driven mainly by the growth of existing microcracks in the isotropic models and by the initiation of new microcracks in the anisotropic models: C) Microcrack area vs. energy dissipation: Anisotropy substantially increased the energy dissipated per microcrack area with the effect being largest for the homogenous case.

Figure 8. Location of microcracks (labeled dots) at a total microcrack area of approximately 2.5 x 10^{-3} mm^2 numbered in order from largest to smallest microcrack in the A) IsoHmg, B) IsoHtg, C) AnisoHmg, and D) AnisoHtg models demonstrated anisotropy alters microcrack locations and heterogeneity alters microcrack area distributions. Transaxial loading direction equals the z-axis.

Figure 9. Individual microcrack growth curves for the A) IsoHmg, B) IsoHtg, C) AnisoHmg, and D) AnisoHtg models demonstrated that while for all models the total microcrack area was driven by a small fraction of the total microcrack number the initial crack dominated the isotropic models. The initial microcrack is denoted by lines with markers and the darker the line the earlier the crack initiated.

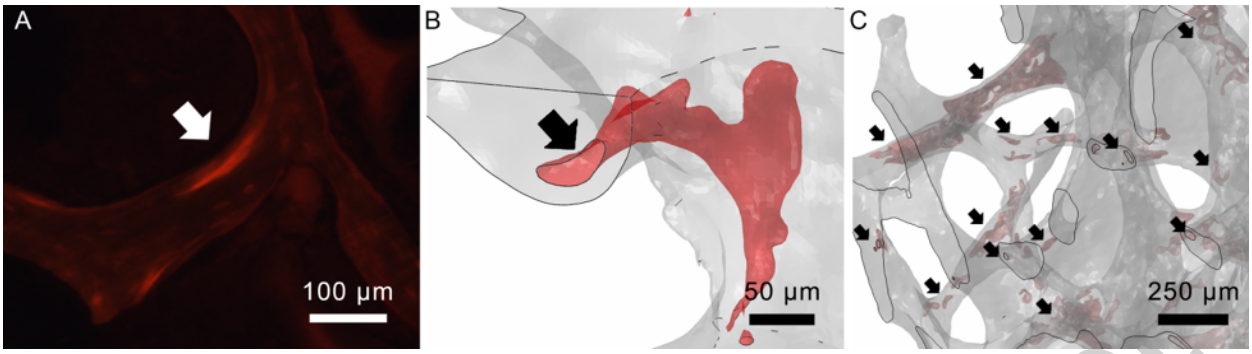

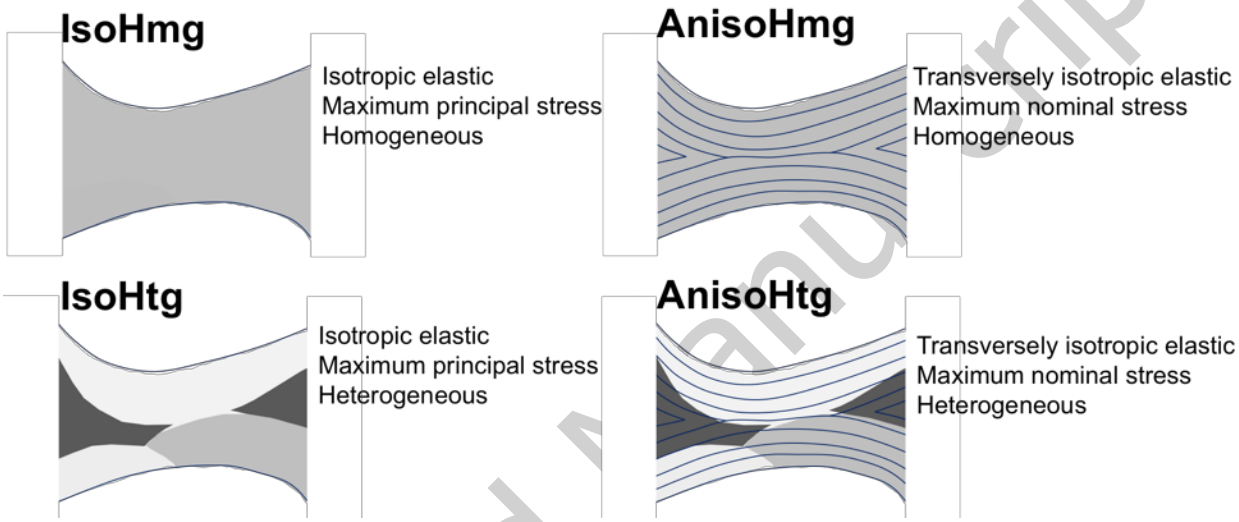

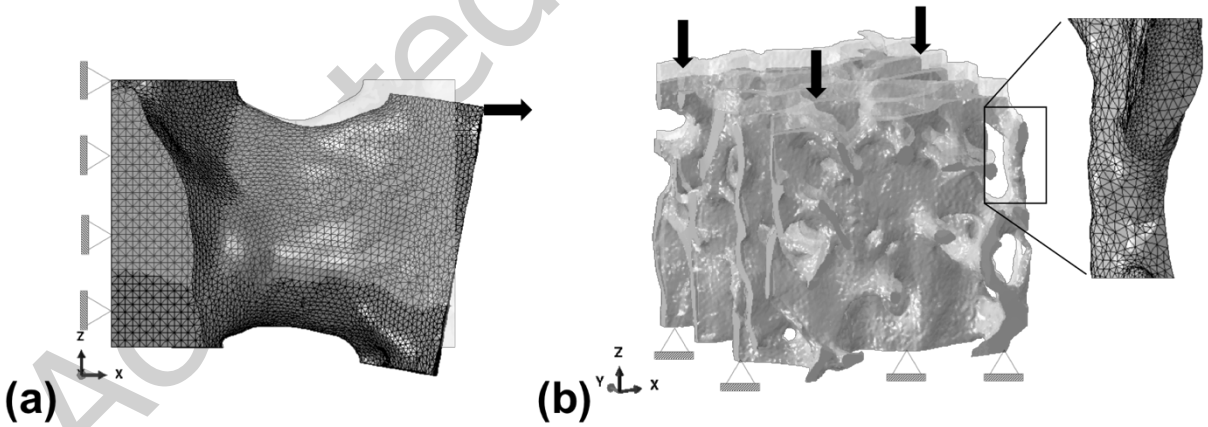

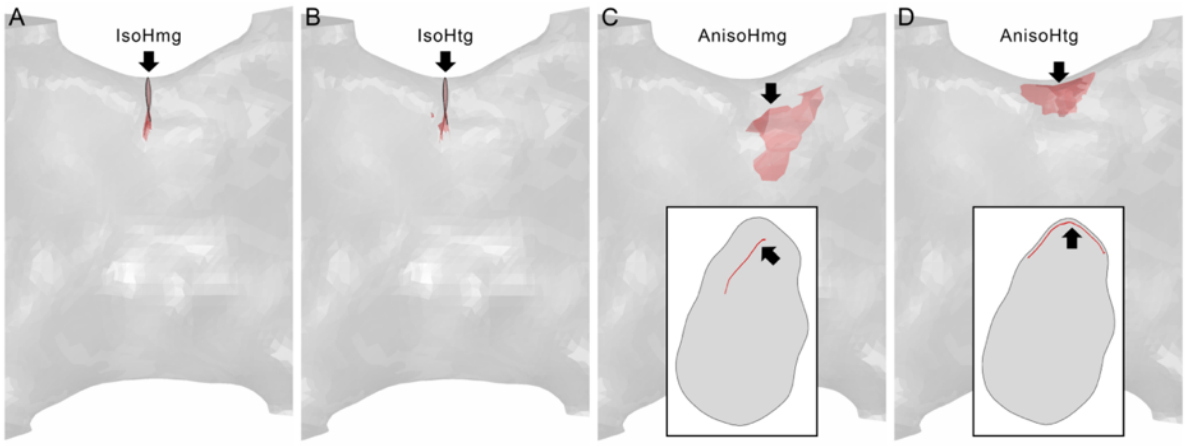

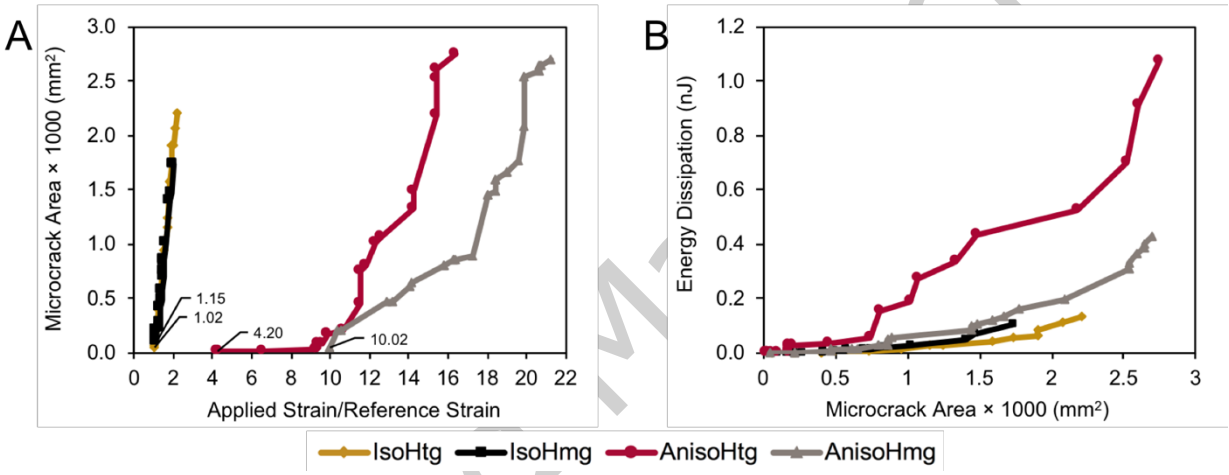

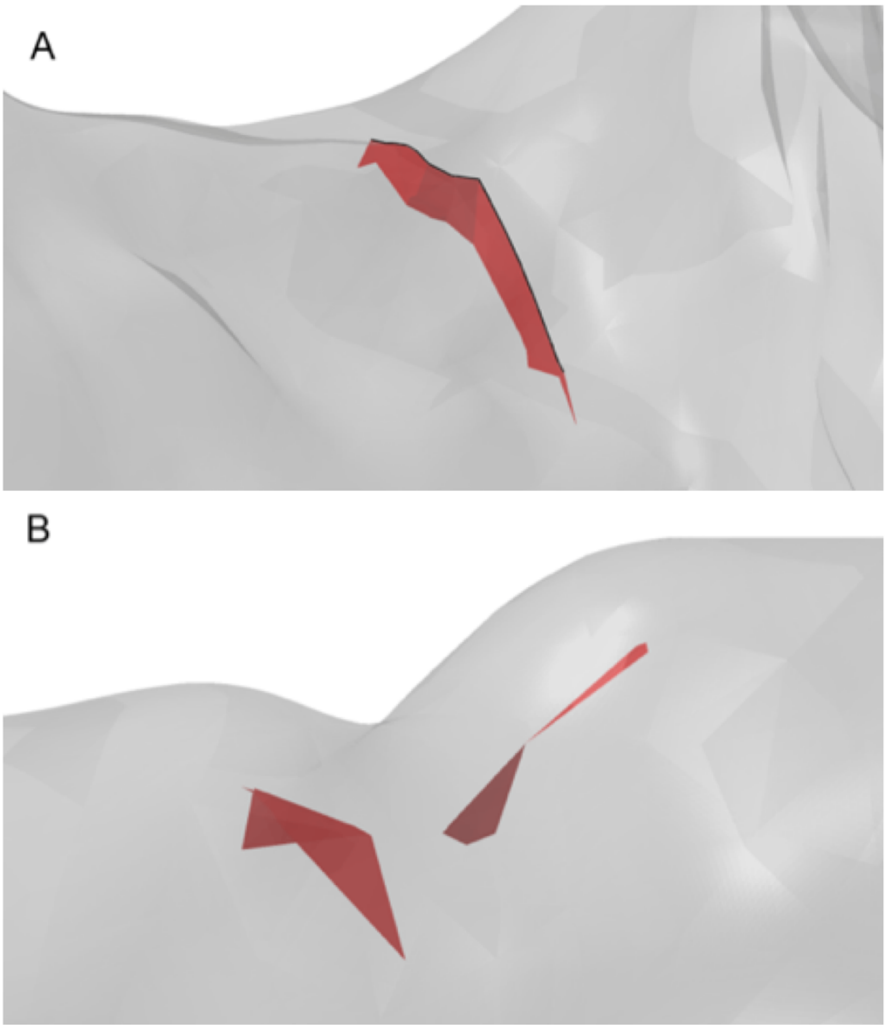
A
B

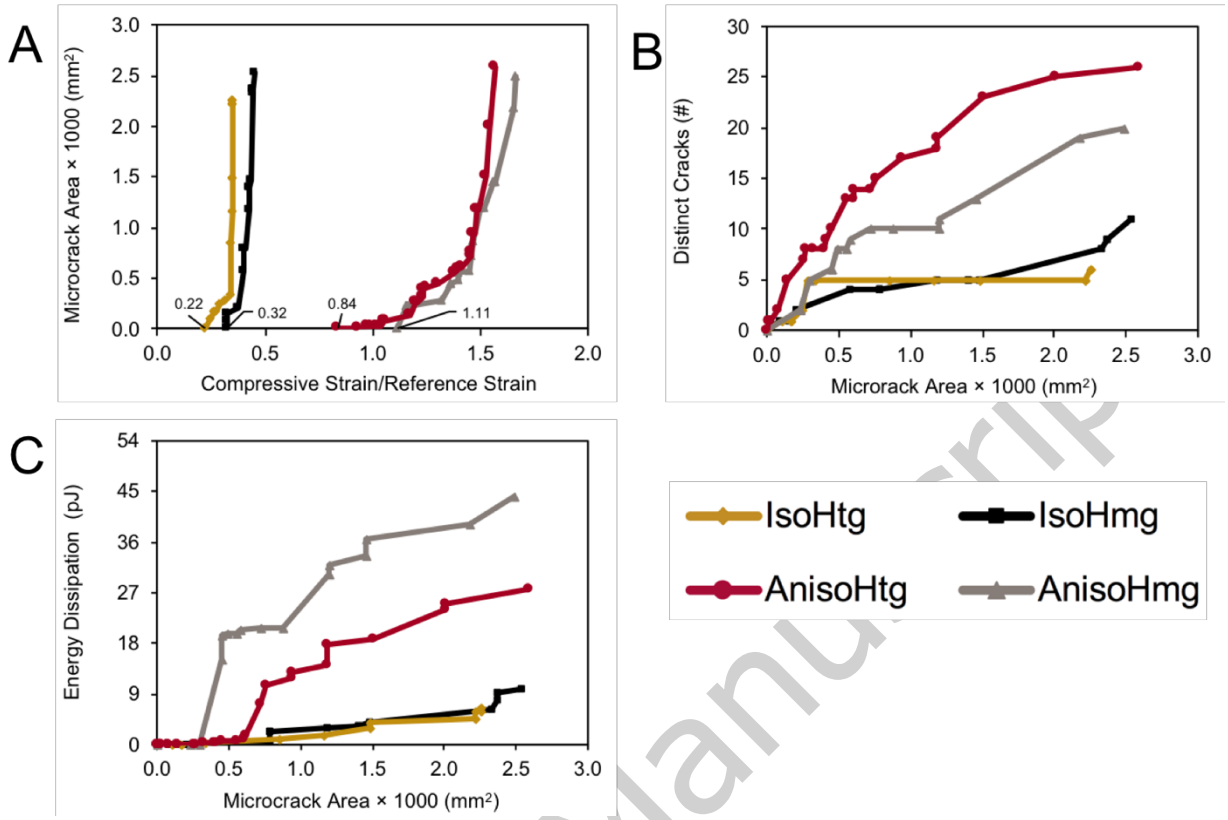

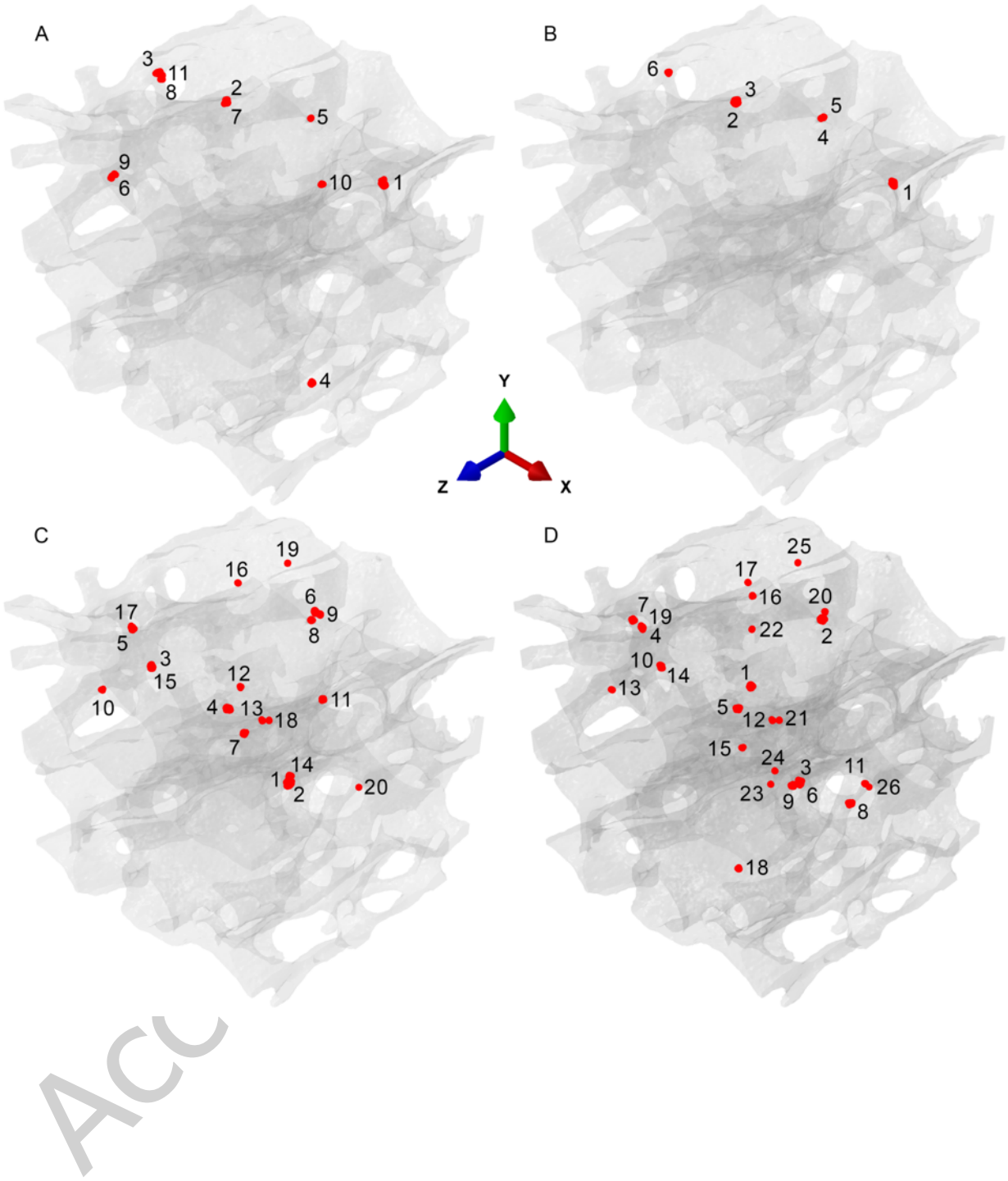
A
3
11
8
2
7
5
9
6
10
1
4
B
6
3
2
5
4
1
Y
Z
X
C
19
16
6
9
8
17
5
3
15
12
10
4
13
18
11
7
14
1
2
20
D
25
17
16
20
7
19
4
22
2
10
14
1
13
5
12
21
15
24
3
11
23
9
6
26
8
18